RSC Advances

PAPER

View Article Online
View Journal | View Issue

Cite this: *RSC Adv.*, 2017, **7**, 29458

Improved sodium-ion storage properties by fabricating nanoporous CuSn alloy architecture†

Ruie Zhang,[a] Zhifeng Wang,[a] Wenqing Ma,[a] Wei Yu,[a] Shanshan Lu[a] and Xizheng Liu *[ab]

Received 31st March 2017
Accepted 23rd May 2017

DOI: 10.1039/c7ra03718j

rsc.li/rsc-advances

Tin-based materials have been considered as promising anodes for sodium-ion batteries because of their high theoretical capacity and low-cost. However, their significant volume expansion and low conductivity prohibit their practical applications. A novel CuSn alloy composite with three-dimensional nanoporous structure was prepared by the dealloying method, which can be easily scaled up for mass production. The main component after 24 hours of dealloying is $Cu_{6.25}Sn_5$, which displays a bi-continuous structure and the ligament width of 50 nm. The as-prepared nanoporous CuSn alloy composite delivers a capacity of 573.2 mA h g^{-1}. After 100 repeated cycles, the capacity was still 233.2 mA h g^{-1}. This result is much superior to that of pure Sn particles, and the nanoporous structure is well maintained after discharge. The accommodation of volume expansion after discharging, the shortened ion diffusion distance and improved conductivity are expected to facilitate the excellent electrochemical performance. These results demonstrate that the nanoporous CuSn alloy provides unique characteristics for ultrastable sodium-ion battery anodes.

Introduction

Rechargeable sodium-ion batteries (SIBs) have attracted significant attention for large-scale stationary applications because of the abundant sodium resources and similar ion storage mechanism as compared to lithium-ion batteries (LIBs).[1,2] The commercialized LIBs graphite anode does not work in SIBs;[3–6] sodium ions prefer to deposit on the graphite surface rather than intercalate into graphite layers, due to the higher desolvation energy.[7] Tremendous efforts have been made to find suitable anodes for SIBs;[8] carbon materials,[9,10] metal oxides and alloys are the most widely investigated anode materials for SIBs.[11–13] Among these materials, the tin-based alloy type anode is attractive due to its high theoretical capacity of 847 mA h g^{-1} in SIBs.[14–16]

However, the Sn-based anodes experience severe volume expansion (420% for $Na_{15}Sn_4$), which leads to the particles' pulverization and peeling off from the current collector;[17] this precludes the utilization of these high capacity materials and deteriorates the cycle stability. In addition, the low conductivity of the discharged electrode composite also results in poor rate performance.[4,18] To conquer these challenges, Sn/carbon composites have been prepared in which the carbon component improves the conductivity and the void space can accommodate the volume expansion.[19,20] However, the electrochemical inactivity and low sodiation rates of carbon materials prevent the excessive use carbon additive.[4] The surface modification, nanotechnology and deposition of active materials on hierarchical fiber *etc.* have also been developed to alleviate the mechanical strain and enhance their electrochemical performance.[21–24] Wang *et al.* synthesized tin-coated viral nanoforests by using the tobacco mosaic virus as a bio-inorganic template, which exhibited superior electrochemical performance as the anode in SIBs.[25] Hu *et al.* developed a nature inspired, low cost electrode consisting of an electrodeposited Sn film on conductive wood fiber.[26] Both the hierarchical wood fiber substrate and 3D Sn nanoforest afforded lightweight substrates with excellent mechanical properties, and porous structures that provided effective ion and electron transport pathways.[27–29] Recently, Na-active metal-Sn alloys (*e.g.* Ni and Sb *etc.*) have been adopted as SIB anodes, which effectively improved not only the structure stability, but also the conductivity of the electrode composites.[30–33] For instance, Yu *et al.* reported a new type of porous Ni–Sn intermetallic microcage anode for high performance lithium-ion batteries (LIBs) and SIBs.[34] We also developed a highly crystalline CuSi alloy nanoporous composite, which showed ultrastable cycle and high rate performance as the anode in LIBs.[35] The introduction of Cu into Sn-based composites for use as anodes in LIBs can significantly improve the cycle stability and conductivity. More recently,

[a]*Tianjin Key Laboratory of Advanced Functional Porous Materials, Institute for New Energy Materials and Low-Carbon Technologies, School of Material Science and Engineering, Tianjin University of Technology, Tianjin 300384, P. R. China. E-mail: xzliu@tjut.edu.cn*

[b]*Key Laboratory of Advanced Energy Materials Chemistry (Ministry of Education), Nankai University, Tianjin 300071, P. R. China*

† Electronic supplementary information (ESI) available. See DOI: 10.1039/c7ra03718j

$Sn_{0.9}Cu_{0.1}$ nanoparticles have been studied as an anode material for SIBs, and have shown considerably superior electrochemical performance, compared to pure Sn.[36]

Inspired by the aforementioned progress, we herein report the design and fabrication of a unique three-dimensional (3D) nanoporous CuSn alloy composite by dealloying CuSnAl alloy in alkaline aqueous solution.[37] The components and porous structure have been optimized by controlling the etching time. Three advantages have been achieved from this design: first, the structure facilitates the electrolyte permeation and accommodates the volume expansion during battery cycling; second, the presence of Cu improves the electrode conductivity; third, the facile material preparation method enables large scale mass production. Our results demonstrate that the 3D nanoporous CuSn composite shows superior electrochemical performance as the anode in SIBs. The porous structure can be well maintained after repeated discharge/charge cycles.

Experimental

Synthetic procedures

The ternary alloy precursor with nominal composition of $Cu_{17}Sn_7Al_{76}$ (wt%) was prepared by arc melting a mixture of pure Cu (99.99 wt%), pure Sn (99.99 wt%) and pure Al (99.99 wt%) in a high-purity argon gas atmosphere and using Ti getters. The melt spinning method was used to prepare Cu–Sn–Al ribbons. The obtained ribbons in this experiment were 25 μm in thickness and 1.5 mm in width. The nanoporous CuSn alloys were obtained by selectively dealloying Al from ternary CuSnAl alloy in 1 M NaOH aqueous solution at room temperature. As displayed in Fig. 1a, the dealloying time was varied from 12 h to 48 h to optimize the porous structure. The dealloyed samples were washed several times with deionized water and absolute ethanol to remove the residual ions, and then dried at 105 °C in a vacuum. The resulting samples were denoted as CS12, CS24, and CS48 with respect to their etching time, respectively.

Materials characterization

The structure analysis was performed on a Bruker D8 Advance X-ray diffractometer employing a Cu Kα (λ = 0.15418 nm) radiation source. The morphology of the samples was characterized by scanning electron microscopy (SEM, Quanta FEG 250) and transmission electron microscopy (TEM, Tecnai G2). The chemical composition of the samples was estimated by using an inductively coupled plasma emission spectrometer (ICP-AES, Shimadzu). The CSA composites were dissolved in a mixed acid solution ($HCl/HNO_3 = 3:1$), and the quantities of Cu and Sn in the solution were then analyzed by elemental analysis using ICP-AES. The composition of the electrodes after discharging was measured by using an X-ray photoelectron spectrometer (XPS, Escalab 250Xi). BET measurements were performed on a Quadrasorb SI analyser at 77 K. The isotherms obtained from adsorption measurements provided information on the surface area, and N_2 adsorption isotherms provided information on size distributions; a wide range of relative pressures (p/p_0) were applied, and the corresponding pore size model was developed by Barrett–Joyner–Halenda (BJH).

Electrochemical characterization

The electrochemical properties of the samples were evaluated in CR2032 coin-type cells, which were assembled in an argon-filled glove box with less than 0.1 ppm of both moisture and oxygen. The working electrodes were composed of 70 wt% of active material, 20 wt% of acetylene black (AB), and 10 wt% of carboxymethylcellulose sodium (CMC) as a binder. The slurry was then cast on a Cu foil and dried at 120 °C for 24 h in vacuum. The cells were assembled using metallic Na anode, an electrolyte comprised of 1 M $NaClO_4$ in a mixture of ethylene carbonate/diethyl carbonate (1 : 1, by volume), and a glass fiber (GF/D) from Whatman was used as a separator. The mass loading of the active materials was about 1.2 mg cm^{-2}. The galvanostatic cycling test of the assembled cells was conducted on a LAND CT2001A battery test system in a voltage range of 0.05–3.0 V (*vs.* Na/Na^+). Cyclic voltammetry (CV) was carried out on an electrochemical workstation in the potential window of 0.05–3.0 V, at a scanning rate of 0.1 mV s^{-1} (CHI 760E). Electrochemical impedance spectral (EIS) measurements were measured over the frequency range from 100 kHz to 0.01 Hz by applying a sine wave with amplitude of 5 mV.

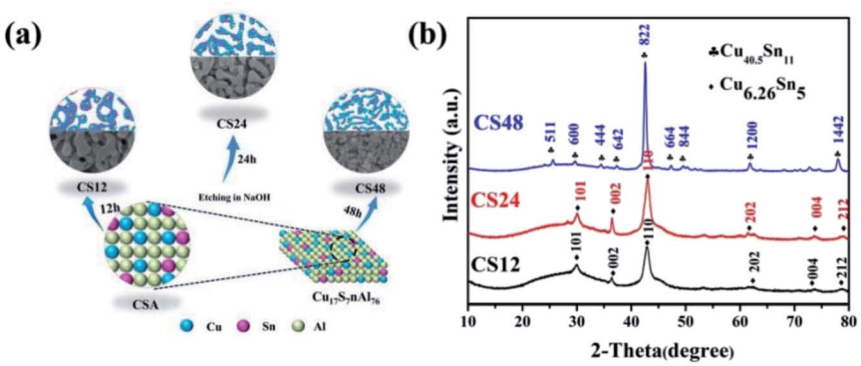

Fig. 1 (a) Schematic for the fabrication procedure of the CSA nanoporous composites. (b) XRD patterns of CSA nanoporous composites with different corrosion time (in 1 M NaOH aqueous solution).

Results and discussion

The crystal structure and phase composition of the alloy precursor were identified by XRD, as shown in Fig. S1;† the CuSnAl phase can be identified. The corresponding morphology was characterized by SEM, as shown in Fig. S2a.† The excess Al contents can be observed as the bright part. The ternary alloy CuSnAl, was then selectively dealloyed in the NaOH solution to etch Al out. As shown in Fig. 1a, the Al was easily etched out initially, while the Sn was gradually corroded only after long time exposure in alkaline solution. We collected the samples after dealloying for 12 h, 24 h and 48 h, and the resulting samples were denoted as CS12, CS24, and CS48, respectively. The compositions of the precursor alloy and various CuSn samples (CS12, 24, 48) are shown in Table S1.† The structures of the as-prepared samples were evaluated by XRD as presented in Fig. 1b. For CS12 and CS24, the diffraction peaks at around 30.1, 35.2, and 42.9 can be assigned to the 101, 002, and 110 crystal planes of the $Cu_{6.26}Sn_5$ phase, respectively (JCPDS# 47-1575), while for CS48, the diffraction peaks at 42.6, 61.8, and 77.9 can be indexed to the 822, 1200, and 1442 crystal planes of the $Cu_{40.5}Sn_{11}$ phase, respectively (JCPDS# 31-0485). This result demonstrates that the corrosion of Sn began with an extension of the corrosion time just beyond 24 h.

For a detailed morphological and structural investigation, we characterized these dealloyed samples by SEM, TEM, and high resolution TEM. As shown in Fig. 2a, S2b and c,† both CS12 and CS24 demonstrate a porous morphology with many large pores distributed on the surface. After extending the dealloying time to 48 h, the resulting sample CS48 evolved into roughened ligaments and atypical pores (Fig. S2c†). The TEM images shown in Fig. 2b and S3† also clearly reveal the porous features of the dealloyed samples. The characteristic lattice spacing of $Cu_{6.26}Sn_5$ (101 002) indicates the good crystallinity of CS24 (Fig. 2c); therefore, the porous structure with conductive Cu framework was obtained as designed.

N_2 adsorption–desorption isotherms were obtained to determine the Brunauer–Emmett–Teller (BET) specific area and Barrett–Joyner–Halenda (BJH) pore size distribution, as shown in Fig. S4.† Fig. S4a† illustrates the N_2 adsorption isotherms and corresponding pore size distribution curves of CS12. The isotherms show two hysteresis loops at relative pressures (p/p_0) ranging from 0.65 to 0.98, indicating a bi-modal pore size distribution (both of mesopores and macropores). Fig. S4b and c† show the corresponding curves of CS24 and CS48; most of the isotherms are type IV curves, which exhibit mesoporous characteristics.[38–40] The specific surface areas are 29.827 $m^2\ g^{-1}$, 29.340 $m^2\ g^{-1}$, and 33.105 $m^2\ g^{-1}$ for CS12, CS24 and CS48, respectively. The porosity increased with the increased corrosion time, consistent with the SEM results.

The structural features of the designed nanoporous CuSn alloys led to their superior electrochemical performance as anodes in SIBs, which was evaluated in coin-type cells at room temperature. The discharge/charge curves at the initial cycle of the CSs are displayed in Fig. 3a and S5.† At a current density of 50 mA g^{-1}, the CS12, CS24, and CS48 display charge capacities of 593.2 mA h g^{-1}, 573.2 mA h g^{-1} and 504.7 mA h g^{-1}, respectively. For comparison, the cycle performance of commercial Sn and nanoporous CSs are shown in Fig. 3b and S6.† The specific capacities of CS12 and CS48 decayed rapidly during the 100 cycles, and only a capacity of 141.6 mA h g^{-1} and 96 mA h g^{-1} remained, respectively. However, such a cycling stability is still much higher than that of the commercial Sn particles (31.3 mA h g^{-1}). The CS24 demonstrated a much improved cycle stability, compared to the others; it delivered a discharge capacity of 233.2 mA h g^{-1} at the 100th cycle (Fig. S7†).

Furthermore, the CS24 exhibited a good rate performance, where the reversible capacities of 365.6, 241.4 and 207.3 mA h g^{-1}, were achieved at the current densities of 100, 150, and 200 mA g^{-1}, respectively (seen Fig. 3c). It should be noted that, when the current density was switched back to 50 mA g^{-1}, a high capacity of 343 mA h g^{-1} was retained. The cycle and rate performance could be ascribed to the 3D porous conductive framework, which highly improved the structure sustainability and electric/ionic conductivity. The appropriate porous structure, component ratio and surface morphology are important for sodium storage properties. We also carefully compared the electrochemical performance with that of Sn-based materials in

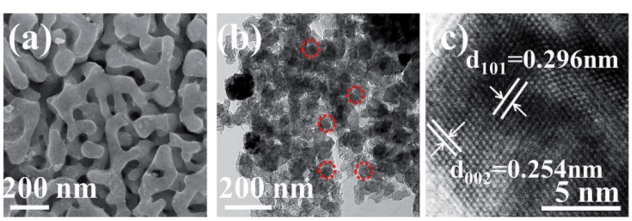

Fig. 2 Characterizations of CuSn anodes: (a) SEM image of nanoporous CS24, (b) low-magnification TEM of CS24 showing bi-continuous porous structures, and (c) HRTEM image of CS24.

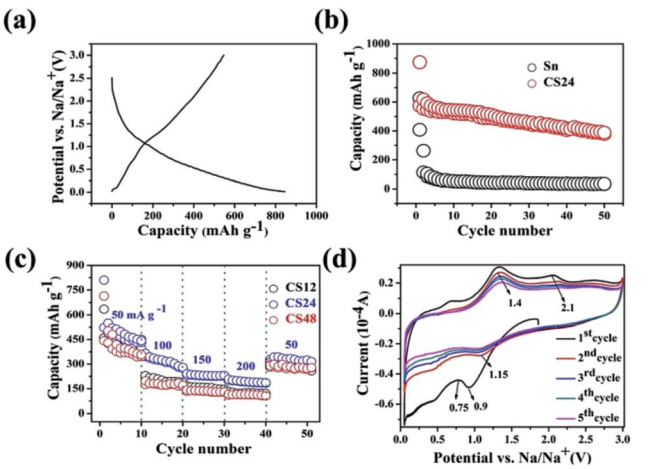

Fig. 3 Electrochemical performances of CSA nanoporous composites in SIB: (a) The first cycle discharge/charge curves of CS24 at 50 mA g^{-1}. (b) Cycling performance of CS24 and pure Sn anodes at 50 mA g^{-1}. (c) Rate capabilities of CS12, CS24, and CS48 electrodes at different current densities from 50 to 200 mA g^{-1}. (d) CV curves of 1–5 cycles of the CS24 electrode at a scan rate 0.1 mV s^{-1} in the potential range from 0.05 to 3.0 V *vs.* Na/Na^+.

Table 1 Summary of Sn and Sn based electrodes materials for Na-ion battery applications

Material	Synthesis method	First charge capacity (mA h g^{-1} (A g^{-1}))	Capacity (mA h g^{-1})/(cycles)	CE in first cycle	Capacity at a high rate (mA h g^{-1} (A g^{-1}))	Ref.
Sn film on natural wood fiber	Electrodeposition	339(0.084)	145(400)	23%	200(0.084); 130(0.168); 50(0.84)	26
Sn–Ni intermetallic microcages	Solvothermal	384(0.6)	280(300)	35.5%	447(1.2); 351(3); 276(6)	34
Al_2O_3/Sn NPs@CNF	Electrospinning atomic-layer-deposition	625(0.0847)	650(40)	63.7%	—	41
Sn/graphite composite	Ball milling	410(0.05)	360(20)	70%	—	20
Sn/porous C composite	Thermal reduction	295(0.02)	195(15)	38.8%	200(0.2); 100(0.4); 75(1)	3
Cu_6Sn_5 + TiC + C: no additive	Ball milling	225(0.1)	98(100)	61%	130(0.5); 120(1); 110(3); 80(5)	42
Cu_6Sn_5 + TiC + C: 2 vol% FEC	Ball milling	146(0.1)	137(250)	56%	135(0.3); 130(1); 125(3); 120(5)	42
SnSb/CNT@GS	Hydrothermal technique and chemical vapor deposition	424(100)	360(100)	62%	422(100), 355(200), 301(500), 278(750), 268(1000)	30
$(Cu_6Sn_5)_{1-x}C_x$	Combinatorial sputtering	310(0.1), $x = 0.15$	117(50)	88.5%	—	28
$Sn_{0.9}Cu_{0.1}$	Surfactant-assisted wet	250(0.2)	440(20)	35%	265(0.2), 182(1), 126(2)	36
$Cu_{6.26}Sn_5$	**Dealloying**	**573.2(0.05)**	**233.2(100)**	**65.7%**	**522.0(0.05); 365.6(0.1); 241.2(0.15); 207.3(0.2)**	**This work**

SIBs, as shown in Table 1. The present result is obviously superior to that of reported results.

CV measurement of CS24 was conducted in a potential window of 0.05–3 V at a scan rate of 0.1 mV s^{-1}. As shown in Fig. 3d, a broad irreversible peak was initially located at around 0.7 V, which could be assigned to the formation of solid electrolyte interphase (SEI) film on the electrode surface. The other two reduction peaks observed at around 0.05 V and 0.9 V could be ascribed to the sodiated process of the active material. The oxidation peaks were located at about 1.4 and 2.1 V, whereas, as demonstrated, the reduction peaks switched to 0.45 and 1.15 V in the subsequent cycles and remained stable, indicating the reversible sodiation behaviors. This result is consistent with the discharge profiles.

In order to clarify the effect of the Cu framework, we prepared a porous Sn sample from the SnAl alloy precursor with the same conditions and methods of CuSnAl. SEM images of the SnAl alloy before and after etching for 24 h are shown in Fig. S8a and b,† which exhibit porous architecture. XRD patterns determine the crystal structure of the as prepared samples. As illustrated in Fig. S8c,† the main composition of SnAl-24 h is Sn (JCPDS #65-7657). Electrochemical impedance spectroscopy (EIS) was employed to evaluate the detailed electrochemical kinetics of SnAl-24 h electrodes during battery cycling. As seen Fig. S8d,† the Na-ion migration resistance (R_{SEI}) and charge transfer resistance (R_{ct}) of the CS24 cell after 1 cycle are all smaller than the SnAl cell after 1 cycle, indicating that the CS24 has better electrochemical performance; therefore, the Cu components enhanced the conductivity of the electrode composite.

In order to further monitor the discharge process, the surface and inner information evolution of the CS24 electrodes were investigated by XPS. We collected the XPS information of the fresh electrode and discharged electrode. The discharged electrode was also subjected to 2 minutes Ar-ion etching to exclude the surface SEI film effects. The Cu2p and Sn3d spectra are presented in Fig. 4. In the fresh state, the peaks located at 932.4 eV and 952.5 eV can be assigned to Cu2p1/2 and Cu2p3/2 of metallic Cu(0) and oxidized Cu(II), respectively, and the peaks located at 484.9 eV and 494.5 eV can be indexed well to metallic (Sn3d5/2) and oxidized Sn(IV) (Sn3d3/2). The trace oxide layer was formed *in situ* during dealloying in alkaline aqueous solution. After discharging, a new peak located at about 496.3 eV was observed at both the surface and inner electrode. This is ascribed to the sodiation of Sn and formation of the $Na_{15}Sn_4$ alloy after discharging. It is very different for the Cu spectra of the discharged electrode: no Cu could be detected at the surface, while the peaks after Ar-etching appeared at a similar position to the fresh electrode. The sodiation process of CuSn alloys can be inferred from the XPS data: at first, the dealloying of CuSn alloy accompanied the sodiation process, and then the Sn element was enriched at the electrode surface, which is very different from our previous results for the CuSi alloy anode.[35]

To determine the performance improvement mechanism, the cycled CS24 electrodes were characterized by SEM and TEM. The surface morphologies of the fresh electrode and after 10 cycles are displayed in Fig. 5a and b. There was no particle pulverization or peeling off from the current collector. Even

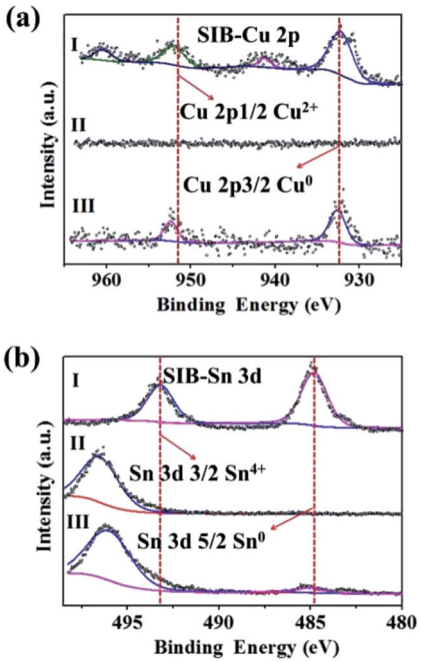

Fig. 4 XPS spectra of Cu2p and Sn3d for (I) the pristine CuSn alloy, (II) the electrode of the first discharge to 0.05 V before etching, (III) the electrode of the first discharge to 0.05 V after 2 min of argon etching.

after 100 cycles, no obvious morphology evolution could be detected, as shown in Fig. S9.† The porous structure accommodated the volume changes during battery cycling. Furthermore, the TEM images shown in Fig. 5c and S10† demonstrate

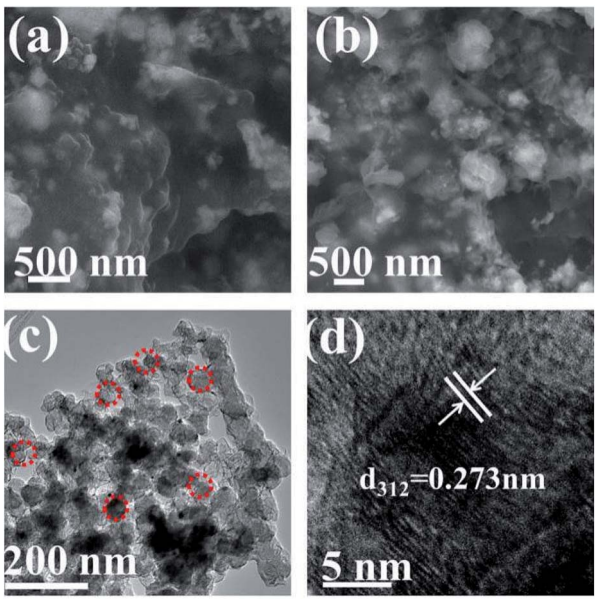

Fig. 5 (a) SEM images of CS24 electrodes before cycles, (b) SEM images of CS24 electrodes after 10 discharge/charge cycles at a current density of 50 mA g^{-1}, and (c) low-magnification TEM image showing well-maintained morphology of CS24 electrode after discharge to 0.05 V, and (d) high-magnification TEM displaying details of CS24 electrode after discharge to 0.05 V at a current density of 50 mA g^{-1}.

the well-defined porous structure after the first discharge. Huang *et al.* found that the first sodiation process occurred in two steps;[17] that is, the crystalline Sn nanoparticles were initially sodiated *via* a two-phase mechanism with a migrating phase boundary to form a Na-poor, amorphous Na_xSn alloy ($x \sim 0.5$), which was further sodiated to several Na-rich, amorphous phases and finally to the crystallized $Na_{15}Sn_4$ ($x = 3.75$) *via* a single-phase mechanism. David Mitlin and Hu's groups also summarized that the high capacities of Sn-based electrode materials are associated with the formation of the $Na_{15}Sn_4$ phase;[7,15] therefore, the lattice fringe spacing of 0.273 nm corresponds to the (312) in crystalline $Na_{15}Sn_4$ (Fig. 5d). This result illustrates that the energy storage mechanism mainly depends on Na–Sn alloying and dealloying. No NaCuSn alloy phase was detected in the HR-TEM image; therefore, we inferred that the dealloying of CuSn and alloying of NaSn occurred simultaneously with the discharging.

Electrochemical impedance spectroscopy (EIS) was employed to evaluate the detailed electrochemical kinetics of the CS24 electrode during battery cycling. Fig. S11† shows typical Nyquist plots of the CS24 electrode before, and after 1 and 10 cycles, which are composed of one depressed semicircle at the high frequency region and a straight sloping line at the low frequency region. The depressed semicircle at high frequency is associated with two overlapping interface impedances (*i.e.*, the electrolyte resistance (R_{SEI}) and charge-transfer resistance (R_{ct})), which correspond to the formation of the solid electrolyte membrane and the charge-transfer reaction, while the low-frequency straight sloping line corresponds to the Na-ion diffusion inside the electrode.[43,44] After cycling, the corresponding resistances became smaller, which demonstrated the formation of a stable SEI and significantly decreased the charge transfer resistance.

Conclusion

In summary, we have proposed a novel 3D nanoporous CuSn composite as a high performance SIB anode. The morphology and components have been tuned by controlling the dealloying time in alkaline aqueous solution. The $Cu_{6.25}Sn_5$, which was dealloyed for 24 hours in 1 M NaOH aqueous solution displayed the high reversible capacity of 573.2 mA h g^{-1}. This result is one of the best obtained for the reported Sn-based SIBs anodes. The bi-continuous structure promotes the electrolyte permeation and accommodates the volume expansion. The Cu components enhance the conductivity of the electrode composite. The CuSn dealloying and NaSn alloying occur during discharging. The enrichment of Sn on the particle surface was verified by XPS after discharging. The superior electrochemical performance, combined with the cost-effective fabrication progress, represents a new strategy for the design and fabrication of high capacity alloy-type anodes for SIBs.

Acknowledgements

This work was financially supported by the National Natural Science Foundation of China (21603162, 51671145), major

projects of new materials of Tianjin city (16ZXCLGX00120), Tianjin Sci. & Tech. Program (17JCYBJC21500), and the Fundamental Research Funds of Tianjin University of Technology.

Notes and references

1 S.-W. Kim, D.-H. Seo, X. Ma, G. Ceder and K. Kang, *Adv. Energy Mater.*, 2012, **2**, 710–721.
2 N. Yabuuchi, K. Kubota, M. Dahbi and S. Komaba, *Chem. Rev.*, 2014, **114**, 11636–11682.
3 Y. Xu, Y. Zhu, Y. Liu and C. Wang, *Adv. Energy Mater.*, 2013, **3**, 128–133.
4 V. L. Chevrier and G. Ceder, *J. Electrochem. Soc.*, 2011, **158**, A1011.
5 M. S. Balogun, Y. Luo, W. Qiu, P. Liu and Y. Tong, *Carbon*, 2016, **98**, 162–178.
6 M. S. B. Jache and D. P. Adelhelm, *Angew. Chem.*, 2014, **53**, 10169.
7 W. Luo, F. Shen, C. Bommier, H. Zhu, X. Ji and L. Hu, *Acc. Chem. Res.*, 2016, **49**, 231–240.
8 S. Komaba, Y. Matsuura, T. Ishikawa, N. Yabuuchi, W. Murata and S. Kuze, *Electrochem. Commun.*, 2012, **21**, 65–68.
9 L. Fu, K. Tang, K. Song, P. A. van Aken, Y. Yu and J. Maier, *Nanoscale*, 2013, **6**, 1384–1389.
10 P. Zheng, T. Liu, X. Yuan, L. Zhang, Y. Liu, J. Huang and S. Guo, *Sci. Rep.*, 2016, **6**, 26246.
11 M. Dahbi, N. Yabuuchi, K. Kubota, K. Tokiwa and S. Komaba, *PCCP Phys. Chem. Chem. Phys.*, 2014, **16**, 15007–15028.
12 Z. Xu, X. Lv, J. Li, J. Chen and Q. Liu, *RSC Adv.*, 2016, **6**, 25594–25600.
13 Y. Kim, K. H. Ha, S. M. Oh and K. T. Lee, *Chemistry*, 2014, **20**, 11980–11992.
14 M. Mortazavi, J. Deng, V. B. Shenoy and N. V. Medhekar, *J. Power Sources*, 2013, **225**, 207–214.
15 Z. Li, J. Ding and D. Mitlin, *Acc. Chem. Res.*, 2015, **48**, 1657–1665.
16 Q. Li, D. Yi, W. Hao, X. Liu and Y. Qian, *Mater. Res. Bull.*, 2002, **37**, 925–932.
17 J. W. Wang, X. H. Liu, S. X. Mao and J. Y. Huang, *Nano Lett.*, 2012, **12**, 5897–5902.
18 J. Mao, X. Fan, C. Luo and C. Wang, *ACS Appl. Mater. Interfaces*, 2016, **8**, 7147–7155.
19 W. Li, L. Zeng, Z. Yang, L. Gu, J. Wang, X. Liu, J. Cheng and Y. Yu, *Nanoscale*, 2014, **6**, 693–698.
20 M. K. Datta, R. Epur, P. Saha, K. Kadakia, S. K. Park and P. N. Kumta, *J. Power Sources*, 2013, **225**, 316–322.
21 W. Li, Y. X. Yin, S. Xin, W. G. Song and Y. G. Guo, *Energy Environ. Sci.*, 2012, **5**, 8007–8013.
22 Z. Chen, Y. Yan, S. Xin, W. Li, J. Qu, Y. G. Guo and W. G. Song, *J. Mater. Chem. A*, 2013, **1**, 11404–11409.
23 L. S. Zhang, L. Y. Jiang, C. Q. Chen, W. Li, W. G. Song and Y. G. Guo, *Chem. Mater.*, 2010, **22**, 414–419.
24 X. Li, Y. Feng, M. Li, W. Li, H. Wei and D. Song, *Adv. Funct. Mater.*, 2015, **25**, 6858–6866.
25 Y. Liu, Y. Xu, Y. Zhu, J. N. Culver, C. A. Lundgren, K. Xu and C. Wang, *ACS Nano*, 2013, **7**, 3627.
26 H. Zhu, Z. Jia, Y. Chen, N. Weadock, J. Wan, O. Vaaland, X. Han, T. Li and L. Hu, *Nano Lett.*, 2013, **13**, 3093–3100.
27 L. H. Qian, Y. Ding, T. Fujita and M. W. Chen, *Langmuir*, 2008, **24**, 4426–4429.
28 J. S. Thorne, R. A. Dunlap and M. N. Obrovac, *Electrochim. Acta*, 2013, **112**, 133–137.
29 G. D. Park, J. H. Lee and Y. C. Kang, *Nanoscale*, 2016, **8**, 11889–11896.
30 K. S. Shiva, H. B. R. Rajendra and A. J. Bhattacharyya, *Chempluschem*, 2014, **80**, 516–521.
31 Y. Zhu, P. Nie, L. Shen, S. Dong, Q. Sheng, H. Li, H. Luo and X. Zhang, *Nanoscale*, 2015, **7**, 3309–3315.
32 Y. Liu, H. Kang, L. Jiao, C. Chen, K. Cao, Y. Wang and H. Yuan, *Nanoscale*, 2015, **7**, 1325–1332.
33 A. Darwiche, M. T. Sougrati, B. Fraisse, L. Stievano and L. Monconduit, *Electrochem. Commun.*, 2013, **32**, 18–21.
34 J. Liu, Y. Wen, P. A. van Aken, J. Maier and Y. Yu, *Nano Lett.*, 2014, **14**, 6387–6392.
35 W. Ma, X. Liu, X. Wang, Z. Wang, R. Zhang, Z. Yuan and Y. Ding, *J. Mater. Chem. A*, 2016, **4**, 19140–19146.
36 Y. M. Lin, P. R. Abel, A. Gupta, J. B. Goodenough, A. Heller and C. B. Mullins, *ACS Appl. Mater. Interfaces*, 2013, **5**, 8273–8277.
37 C. Xu, Y. Li, F. Tian and Y. Ding, *ChemPhysChem*, 2010, **11**, 3320.
38 J. C. Groen, L. A. A. Peffer and J. Pérez-Ramírez, *Microporous Mesoporous Mater.*, 2003, **60**, 1–17.
39 W. Li, D. Chen, F. Xia, J. Z. Y. Tan, P. P. Huang, W. G. Song, N. Nursam and R. A. Caruso, *Environ. Sci.: Nano*, 2016, **3**, 94–106.
40 L. Cao, D. Chen, W. Li and R. A. Caruso, *ACS Appl. Mater. Interfaces*, 2014, **6**, 13129.
41 X. Han, Y. Liu, Z. Jia, Y. C. Chen, J. Wan, N. Weadock, K. J. Gaskell, T. Li and L. Hu, *Nano Lett.*, 2014, **14**, 139–147.
42 I. T. Kim, E. Allcorn and A. Manthiram, *J. Power Sources*, 2015, **281**, 11–17.
43 X. Li, G. Wu, X. Liu, W. Li and M. Li, *Nano Energy*, 2017, **31**, 1–8.
44 X. Li, W. Li, M. Li, P. Cui, D. Chen, T. Gengenbach, L. Chu, H. Liu and G. Song, *J. Mater. Chem. A*, 2014, **3**, 2762–2769.